Seismic shaking in the North China Basin expected from ruptures of a possible seismic gap

Benchun Duan[1] (iD)**, Dunyu Liu[1]** (iD)**, and An Yin[2]**

[1]Center for Tectonophysics, Department of Geology and Geophysics, Texas A&M University, College Station, Texas, USA, [2]Deparment of Earth, Planetary, and Space Sciences, University of California, Los Angeles, California, USA

Abstract A 160 km long seismic gap, which has not been ruptured over ~8000 years, was identified recently in North China. In this study, we use a dynamic source model and a newly available high-resolution 3-D velocity structure to simulate long-period ground motion (up to 0.5 Hz) from possibly worst case rupture scenarios of the seismic gap. We find that the characteristics of the earthquake source and the local geologic structure play a critical role in controlling the amplitude and distribution of the simulated strong ground shaking. Rupture directivity and slip asperities can result in large-amplitude (i.e., >1 m/s) ground shaking near the fault, whereas long-duration shaking may occur within sedimentary basins. In particular, a deep and closed Quaternary basin between Beijing and Tianjin can lead to ground shaking of several tens of cm/s for more than 1 min. These results may provide a sound basis for seismic mitigation in one of the most populated regions in the world.
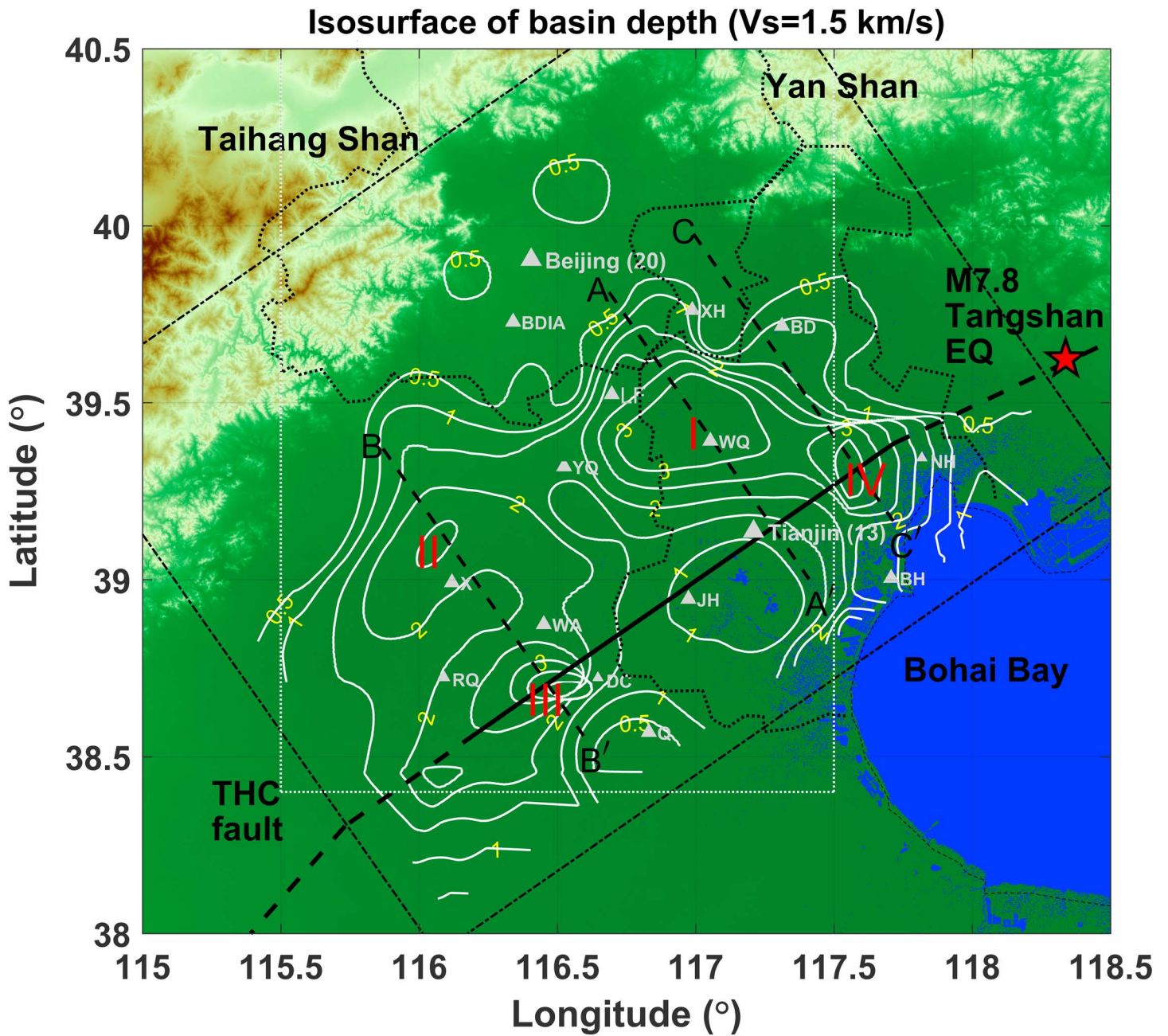
1. Introduction

North China, where the Chinese capital Beijing is located, is prone to large earthquakes, as manifested by a series of M_w 6.0 to M_w 7.8 earthquakes in the 1960s and 1970s [*Liu et al.*, 2011]. Recently, a 160 km long seismic gap (referred to as the Tianjin seismic gap hereafter) along the right-lateral Tangshan-Hejian-Cixian (THC) fault has been identified [*Yin et al.*, 2014]. The devastating 1976 M_w 7.8 Tangshan earthquake, which killed nearly 240,000 people, occurred along this fault directly northeast of the seismic gap (Figure 1). It is estimated that this seismic gap is capable of generating $\sim M_w$ 7.5 earthquakes [*Yin et al.*, 2014]. Tianjin, a city of ~13 million people about 100 km southeast of Beijing, lies atop the seismic gap (Figure 1). Understanding and quantifying the amplitude and distribution of ground shaking due to potential ruptures along this seismic gap are essential for seismic hazard mitigation in this densely populated region.

In this study, we perform dynamic rupture simulations of scenario earthquakes to assess ground-shaking hazards from possibly worst case rupture scenarios, which maximize ground motions, particularly in Tianjin. Dynamic source models can capture abrupt changes in the direction and speed of rupture, features that may be difficult to be characterized in commonly used kinematic source models [*Olsen et al.*, 2008, 2009; *Andrews and Barall*, 2011]. In addition, dynamic source models can incorporate complex physical processes, such as fault roughness, inelastic deformation off the fault, and complex fault frictional behavior, which in turn lead to more accurate characterization of possible near-fault ground shaking [e.g., *Duan and Day*, 2010; *Dunham et al.*, 2011; *Shi and Day*, 2013]. Although several studies attempted to simulate ground motion in the Beijing/Tianjin region [e.g., *Ding et al.*, 2004; *Pan et al.*, 2006; *Zhou and Chen*, 2008; *Liu and Li*, 2011], they did not incorporate high-resolution 3-D basin structures that can potentially amplify and prolong ground shaking. We address this issue by integrating a state-of-the-art dynamic source model with the newly available high-resolution 3-D basin structures to assess seismic hazards in North China imposed by the Tianjin seismic gap.

2. Method and Models

We use a finite element method (FEM) EQdyna to simulate dynamic rupture on the fault and seismic wave propagation in the medium [*Duan and Oglesby*, 2006; *Duan and Day*, 2008; *Duan*, 2010, 2012]. The approach has been verified in a community-wide code validation effort [*Harris et al.*, 2009, 2011]. The perfectly matched layer (PML) absorbing boundary condition [*Berenger*, 1994; *Collino and Tsogka*, 2001; *Ma and Liu*, 2006] and the coarse-grained Q attenuation model [*Day*, 1998] are implemented and verified against a previous study [*Ma and Liu*, 2006]. The main ingredients of a dynamic source model include a geological structure, initial

Figure 1. The Tianjin seismic gap and basin structure of the study area (dash-dotted black rectangle) in the North China Basin. Color background shows topography of the region. The seismic gap (the heavy solid black line) is a 160 km long segment along the Tangshan-Hejian-Cixian (THC) fault (the heavy line), which hosted the deadly 1976 M 7.8 Tangshan earthquake (red star). The white dotted box (with the north edge outside of the map) delimits the region with high-resolution V_p velocity structure (see text). Contour lines are the isosurface depth of the S wave velocity = 1.5 km/s in the study area. I, II, III, and IV are four sedimentary basins. AA', BB', and CC' are three profiles for displaying synthetic seismograms. The North China Basin is surrounded by Bohai Bay, Yan Shan, and Taihang Shan to the east, northeast, and northwest, respectively. Dotted black lines outline the boundaries among Bejing District, Tianjin District, and Hebei province. Numbers following Beijing and Tianjin are approximate populations (in millions). Other cities and places in the study area include BDIA (the Beijing Daxing International Airport), BD (Baodi), BH (Binhai), DC (Dacheng), LF (Langfang), JH (Jinghai), NH (Ninghe), Q (Qingxian), RQ (Renqiu), WA (Wenan), WQ (Wuqing), X (Xiongxian), XH (Xianghe), and YQ (Yongqing).

stresses, a failure criterion, and a friction law that controls how the frictional coefficient evolves during dynamic slip [e.g., *Harris et al.*, 2009].

The North China Basin (Figure 1) underwent several phases of rifting deformation and postrifting subsidence during the Mesozoic and Cenozoic [*Ye et al.*, 1985]. The most recent Cenozoic rifting has resulted in the formation of four major basins (labeled as I, II, III, and IV) in our study area illustrated by the isosurface depth of
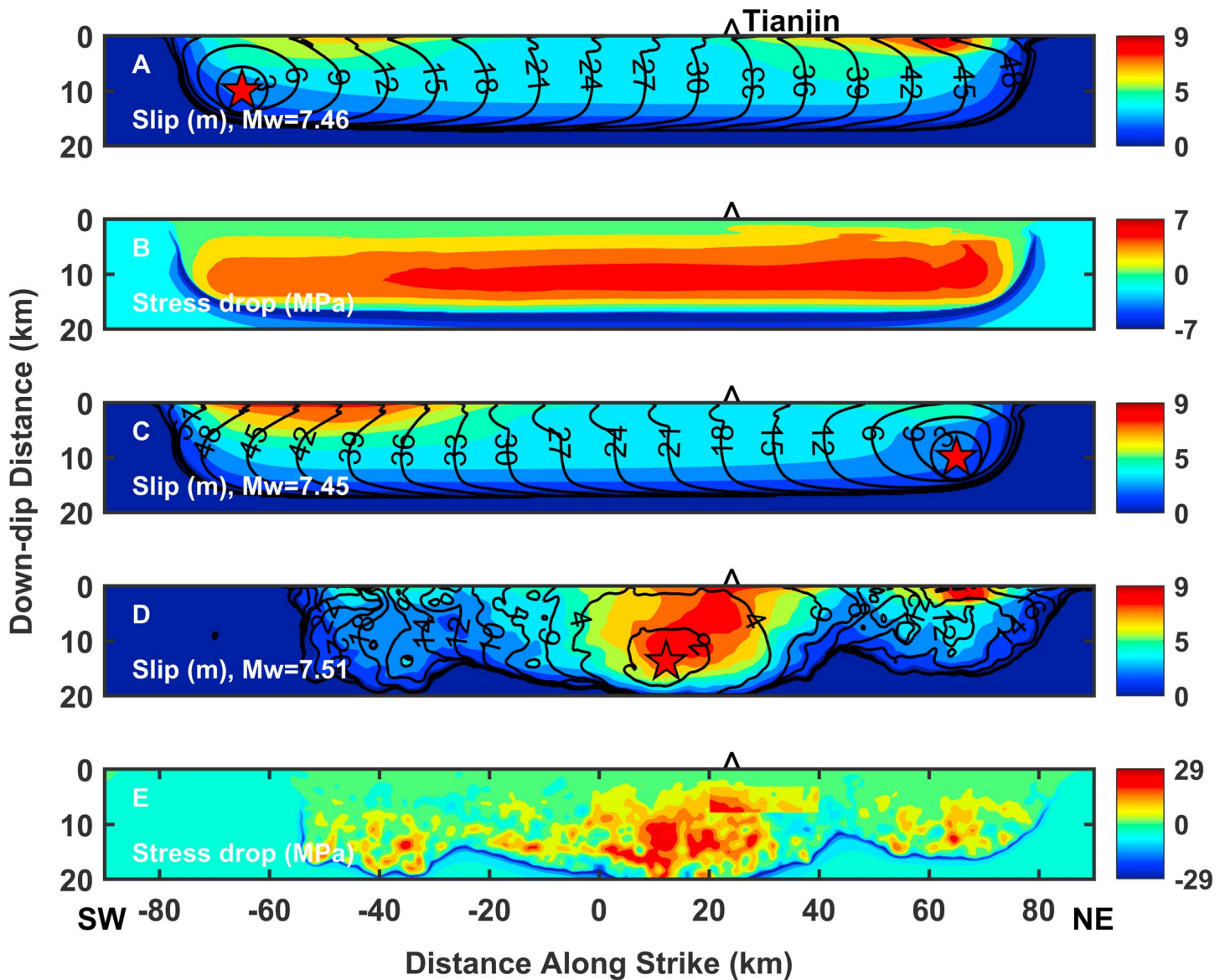
V_s = 1.5 km/s (Figure 1). The crustal structure adopted in this study is constructed as follows. Within the volume of (115.50°E–117.6°E), (38.4°N–40.75°N) and 10 km depth, we use a high-resolution 3-D P wave velocity (V_p) model of *Yang and Huang* [2013]. The resolution of the V_p model is 1 km and 0.1 km along the horizontal and vertical directions, respectively [*Yang and Huang*, 2013]. This V_p model is constrained by industry seismic data. Outside the volume, we use the low-resolution model of *Wei et al.* [2007] to constrain the V_p distribution. S wave velocity (V_s) and crustal density are derived from the P wave velocity using the empirical relations of *Brocher* [2005]. Basins I, II, and III are robust features, whereas the east edge of Basin IV is uncertain as it is located outside the high-resolution V_p domain. Basin I is deep and wide, covering a roughly circular area with a radius of ~25 km at a depth of 3 km (characterized by the V_s = 1.5 km/s isosurface), which contrasts to shallow Basin II and narrow Basins III and IV. Following the attenuation model of *Olsen et al.* [2003], we assume $Q_s = 0.02V_s$ if $V_s \leq 1.5$ km/s, $Q_s = 0.1V_s$ if $V_s > 1.5$ km/s, and $Q_p = 1.5Q_s$. The seismic gap passes through Basins III and IV near its southwest and northeast ends, respectively, whereas the majority of the seismic gap lies within a horst between the two basins (Figure 1). The minimum shear wave velocity in our models is truncated at 500 m/s. Given the uniform finite element size of 200 m, we resolve frequency contents in ground motion up to 0.5 Hz. To resolve higher frequencies that are more relevant to buildings and infrastructure requires finer element sizes and higher resolutions of velocity structure, which are beyond the scope of this study. Each of our models has about 480 million finite elements. With a simulation time of 200 s, each run takes about 22 h using 256 cores and 540 GB memory on a cluster system with Intel's 64 bit 2.8 GHz Nehalem processors.

The Tianjin seismic gap is a relatively straight segment [*Yin et al.*, 2014] and is assumed to be a 20 km deep vertical plane as indicated by earthquake locations [e.g., *Liu et al.*, 2016]. We use the Coulomb failure criterion [e.g., *Scholz*, 2002] to determine whether or not a fault point fails. A linear slip-weakening friction law [*Ida*, 1972; *Andrews*, 1976; *Day*, 1982] is adopted to govern how the frictional coefficient on the fault evolves during dynamic slip, in the form of $\mu(\delta) = \mu_s - (\mu_s - \mu_d)\min(\delta, D_0)/D_0$, where δ is fault slip and D_0 is the critical slip distance over which the static friction μ_s drops to dynamic friction μ_d. A uniform distribution of $D_0 = 0.4$ m on the fault, a value that may be larger than experimentally determined values but is necessary for resolving numerically the cohesive zone at the rupture front [e.g., *Day et al.*, 2005], is used in all model runs. We choose $\mu_s = 0.7$ and $\mu_d = 0.6$ on the fault in the uniform stress ratio models and allow their variations in the self-similar stress model (see below for definitions and details). These values are chosen to satisfy Byerlee's law of friction [*Byerlee*, 1978] and to control stress drop in the slip-weakening friction law, though laboratory high-speed friction experiments suggest lower values for μ_d [e.g., *Di Toro et al.*, 2004].

We follow the procedure proposed by *Andrews and Barall* [2011] to set up the initial fault stress in our models. First, a depth-dependent effective normal stress is assigned on the fault. Second, a ratio μ_0 smaller than 1 between the initial shear and normal stresses is used to characterize the distribution of the initial shear stress on the fault. By adjusting the ratio μ_0 (and dynamic friction μ_d), we control the stress drop distribution that dictates the slip distribution and the seismic S value that dictates the rupture propagation in the models. The seismic S value is defined as $S = (\tau_u - \tau_0)/(\tau_0 - \tau_f)$, where τ_u is the yield stress, τ_0 is the initial shear stress, and τ_f is the sliding frictional stress [*Das and Aki*, 1977]. The S value characterizes how close the fault is to failure under the initial stress field.

In this study, our primary goal is to explore worst case rupture scenarios by quantifying how severe ground shaking can be generated from ~M_w 7.5 earthquakes on the seismic gap, in particular in the city of Tianjin. To this end, we consider two types of the μ_0 distribution. One is uniform, which maximizes the directivity effect when a rupture initiates at one end of the fault. Two scenarios are generated from this uniform μ_0 distribution with nucleation at either the southwest (SW) or the northeast (NE) end of the seismic gap, respectively (Figure 2). We denote them as the uniform stress ratio scenarios and differentiate them by the rupture directions (i.e., the SW-to-NE versus NE-to-SW scenarios, respectively) hereafter. Notice that the only difference in these two uniform stress ratio scenarios is the hypocenter location.

The second type of μ_0 distribution is random and self-similar [*Andrews and Barall*, 2011], which can generate stochastic slip distributions compatible with seismological observations of recent large earthquakes [*Mai and Beroza*, 2002]. Many possible scenarios may be generated from random and self-similar μ_0 distribution (Figure S1 in the supporting information), but we report here only one with a large concentrated slip patch (i.e., an asperity) beneath Tianjin (Figure 2), which may represent the worst case scenario for the city. In this
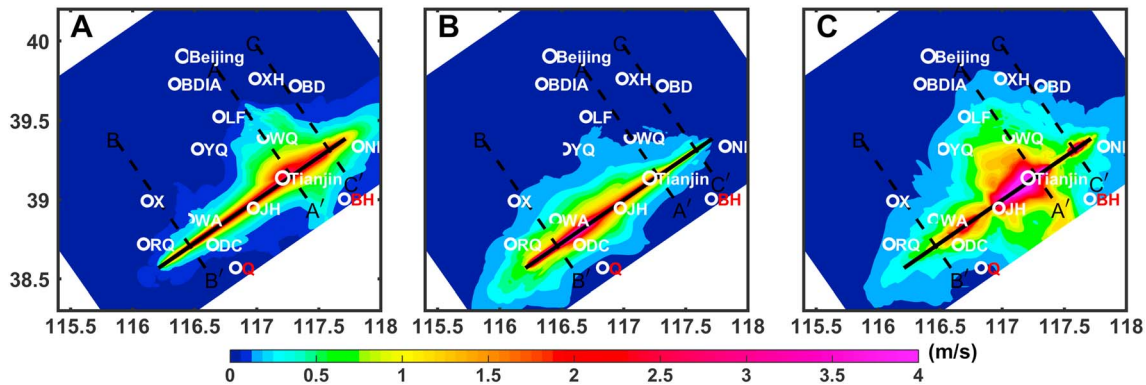
Figure 2. The three rupture scenarios on the Tianjin seismic gap simulated in this study. (a, c) Distributions of slip (color scales) and rupture time (contours in sec) on the fault in the SW-NE and the NE-SW uniform stress ratio scenarios, respectively. (b) The stress drop distribution from the SW-NE uniform ratio stress scenario. (d) The distribution of slip and rupture time in the self-similar stress scenario; (e) distribution of stress drop from the scenario. See text for details of these rupture scenarios.

self-similar stress scenario, μ_s varies from 0.7 to 0.79 to prevent any failure from occurring in the initial stress field [*Andrews and Barall*, 2011]. In addition, μ_d is reduced from 0.6 to 0.5 to produce larger stress drop and thus larger slip within the asperity. We denote this scenario as the self-similar stress scenario. Figure S1 shows the initial normal stress and the initial shear stress for the three scenarios mentioned above and an additional self-similar case.

3. Three Simulated Rupture Scenarios

In dynamic source models, we need a procedure to initiate rupture [e.g., *Andrews*, 1976; *Day*, 1982]. In this study, we initiate a rupture by forcing it to propagate at a fixed speed (i.e., 1.5 km/s) within a 4 km radius circular patch around a preset hypocenter. Outside this initiation patch, rupture propagates spontaneously, which is controlled by the Coulomb failure criterion, the slip-weakening friction law, and the time-

Figure 3. The distribution of the horizontal peak ground velocity (PGV) from the (a) SW-NE uniform stress ratio, (b) NE-SW uniform stress ratio, and (c) self-similar stress scenarios. The PGV value here is the peak value of the amplitude of the horizontal ground velocity from the simulations. Three profiles and cities are the same as in Figure 1.
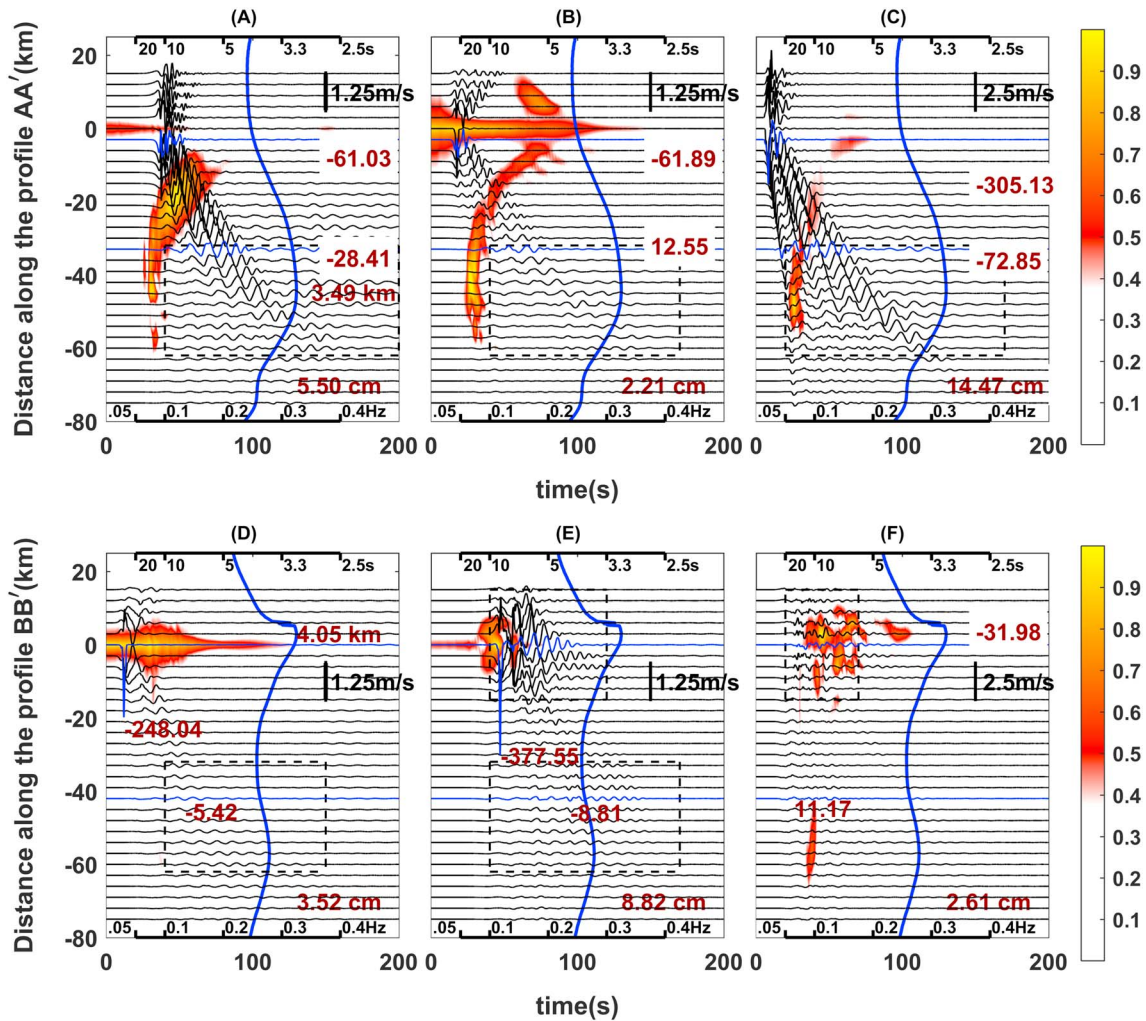
dependent stress field. Rupture propagation in the two uniform stress ratio scenarios is smooth, with a relatively slower speed in the two basins (Basins III and IV) at shallow depth (Figures 2a and 2c). Slip distribution from the two scenarios is similar, characterized by larger fault slip magnitude within the two basins at shallow depths (Figures 2a and 2c). Stress drop distributions from the two scenarios are similar and smooth (Figure 2b).

Stress drop in the self-similar stress scenario is much more heterogeneous (Figure 2e) when compared against the uniform stress ratio scenarios (Figure 2b), which results in complex rupture propagation (Figure 2d). In this scenario, we nucleate rupture at the edge of the largest stress drop patch, which is consistent with seismological observations [e.g., *Mai and Beroza*, 2002]. The rupture propagates near the hypocenter rapidly due to large stress drop, generating an asperity with a peak slip of ~9 m beneath Tianjin. Rupture slows down and even pauses when it propagates into small stress drop patches on the two sides of the asperity (Movie S1). Large shallow slip (i.e., ~5 m) is also observed in Basin IV, whereas the rupture dies out in Basin III in this scenario. Although slip distribution and rupture propagation are significantly different between the self-similar stress scenario and the two uniform stress ratio scenarios, their magnitudes are similar (i.e., ~M_w 7.5).

4. Simulated Ground Motions

The distribution of the horizontal peak ground velocity (PGV) from the two uniform stress ratio scenarios shows clearly a directivity effect, while that from the self-similar stress scenario exhibits strong effects of the asperity on PGV (Figure 3). In all three scenarios, large PGV values (i.e., 0.5 m/s or higher) occur near the fault, but the extent of the large PGV region (outlined by green color) is modulated by the directivity effect and the basin effect. The extent of the large PGV region increases toward the NE in the SW-to-NE rupture scenario (Figure 3a) and toward the SW in the NE-to-SW rupture scenario (Figure 3b). Tianjin experiences larger PGVs in the SW-to-NE scenario than in the NE-to-SW scenario. The basin amplification effect enlarges the extent of the large PGV area, in particular in Basin I between Beijing and Tianjin (Figure 1), suggesting that details of basin effects on PGV depend on the basin shape, depth, location, and size. For example, Basin I is a relatively big and deep basin with a closed geometry, exerting a strong effect on PGV, whereas Basin II is a relatively shallow and open basin with a moderate effect on PGV. The self-similar stress scenario shows strong effects of the asperity on PGV, which produces a ~30 km by 10 km zone of strong shaking with PGVs of ~4 m/s surrounding the city of Tianjin (pink color in Figure 3c). The amplification effect of Basin I superimposes onto the asperity effect in this scenario, resulting in a much wider region of large PGVs than that in the two uniform stress ratio scenarios. In addition, Basins III and IV along the fault generate the other two strong PGV zones along the fault.

The basins in the area cause amplification and prolongation of ground shaking, as shown in the fault-parallel horizontal velocity seismograms along the two profiles AA′ and BB′ (Figure 4). These effects are augmented by the rupture directivity and/or the asperity of the earthquake source. Strong ground shaking of tens of cm/s

Figure 4. Fault-parallel horizontal velocity seismograms (black waveforms) and their spectral amplitudes (color scales) along Profiles AA′ (top row) and BB′ (bottom row, see Figure 1 for the profiles' locations) from the (a, d) SW-NE uniform stress ratio, (b, e) NE-SW uniform stress ratio, and (c, f) self-similar stress scenarios. The positive direction of the vertical axes is southeast along the profiles. Notice that different scales are used for waveforms in different scenarios. Peak velocity values (maroon color, in cm/s) are labeled for two blue traces along each profile. Spectral amplitudes are normalized by the peak value (in centimeters) given at the right bottom corner in each panel. The color scale is designed to clearly show dominant frequency contents in colors, and the period and frequency axes are at the top and bottom of each panel, respectively. Heavy blue curves along the profiles show the isosurface depth of 1.5 km/s wave velocity, with the maximum depth (in kilometers) given in Figures 4a and 4d. Dashed rectangles roughly outline the basin effect on ground velocity, including amplification and/or prolongation.

or larger can last more than a minute in Basin I (Figures 4a and 4c and Wuqing in Figure S4) and Basin III (Figures 4e and 4f and Dacheng in Figure S4). The long duration of strong ground shaking could be destructive to major infrastructure and buildings. A large spike of 377.55 cm/s on the fault in the NE-to-SW scenario (Figure 4e) results from the enhancement between the NE-to-SW rupture directivity and the basin III effect. The effects of Basin II are relatively modest (Figures 4d–4f) on waveforms, as in the PGV case. The effects of Basin IV (Figure S2 in the supporting information) are similar to those of Basin III. These effects of the source characteristics and the basin structure on ground shaking may be more clearly seen in Movie S1 that shows fault rupture propagation and ground motion of the self-similar stress scenario.

The dominant frequencies in the simulated ground motion vary with the locations and the rupture scenarios, as shown by the spectral amplitude of the fault-parallel horizontal ground velocity (colors in Figure 4). Overall, the stations near the fault experience a broader bandwidth of ground shaking, including more high-frequency shaking, while the dominant frequencies for the stations away from the fault are narrowly banded with less high-frequency contents, which is consistent with seismic wave attenuation. The spectral amplitude in Basin I (Figures 4a–4c) is similar to or even larger than that near the fault, indicating the strong effect of

Basin I on ground shaking. Roughly, dominant frequencies in Basin I are within a narrow band of low frequency between 0.06 Hz and 0.09 Hz. The maximum spectral amplitude in the fault-parallel horizontal ground motion (14.47 cm) occurs in the self-similar stress scenario, which is several times larger than that in the other two scenarios.

The fault-normal horizontal component of ground shaking (Figure S3) has comparable amplitudes and durations in the waveforms to the fault-parallel horizontal component. The dominant frequencies exhibit a similar dependence on the locations and the rupture scenarios. In this component, the SW-to-NE rupture scenario produces the largest value of the spectral amplitude (22.34 cm) in Basin IV, suggesting a strong rupture directivity effect in the fault-normal horizontal component near the fault and an enhancement of the rupture directivity by the basin structure.

5. Discussion

Our work shows how earthquake source (e.g., rupture directions and large slip patches) and local geologic structures (e.g., sedimentary basins) control the amplitude, duration, and distribution of ground shaking. Based on the above results, we discuss the impacts of the potential earthquake ruptures along the Tianjin seismic gap. The three-component time histories of ground velocity at the centers of the four cities Beijing, Tianjin, Wuqing, and Dacheng are shown in Figure S4. Ground shaking in Beijing and its surrounding area, including the new airport BDIA (see Figure 1 for location), is weak (i.e., <0.1 m/s) from the scenario earthquakes on this seismic gap, probably due to the relatively thin sediment layer beneath Beijing, the long distance (~100 km) from the source fault, and/or seismic energy emitted from the seismic gap being trapped by Basin I. Because Tianjin sits directly on top of the seismic gap, several m/s of ground velocity in the city can be generated by the potential earthquakes on the gap. Wuqing is at the center of Basin I, and large-amplitude (i.e., ~0.5 m/s) and long-duration (i.e., >1 min) ground shaking can occur. Existence of Basin III and rupture directive may also generate severe ground shaking in Dacheng. All these features can be clearly seen from the synthetic seismograms in Figure S4.

Our modeling efforts here focus on worst case rupture scenarios and neglect other possible scenarios along the Tianjin seismic gap, which may include buried ruptures (in contrast to surface ruptures in this study) that may produce overall lower amplitudes of ground shaking. In addition, inelastic response of rocks and nonlinear response of soils to dynamic rupture and large-amplitude seismic waves, which are ignored in this study, may also reduce ground motion, as shown by recent studies [e.g., *Shi and Day*, 2013; *Roten et al.*, 2014]. More efforts are needed to assess most likely ground motion that can be generated by the seismic gap.

6. Conclusions

Our work demonstrates how a potential $\sim M_w$ 7.5 earthquake on the Tianjin seismic gap in the densely populated North China basin could produce severe ground shaking and how local sedimentary basins with recent Quaternary deposits may affect that shaking. The self-similar stress scenario may be considered as the worst scenario for Tianjin, as a large asperity exists directly beneath Tianjin in this potential earthquake. The SW-to-NE uniform stress ratio scenario could also generate severe shaking in Tianjin because of the directivity effect. The NE-to-SW uniform stress ratio scenario may be considered as the worst scenario for the region near the SW end of the seismic gap, such as the city of Dacheng. The basin between Beijing and Tianjin (Basin I) amplifies and prolongs ground shaking significantly. Existence of Basins III and IV at the two ends of the seismic gap enhances the rupture directivity. These source- and basin-dominated ground-shaking features suggest the importance of scenario earthquake simulations for seismic hazard analysis and mitigation.

References

Andrews, D. J., and M. Barall (2011), Specifying initial stress for dynamic heterogeneous earthquake source models, *Bull. Seismol. Soc. Am.*, *101*(5), 2408–2417, doi:10.1785/0120110012.

Andrews, D. J. (1976), Rupture velocity of plane strain shear cracks, *J. Geophys. Res.*, *81*, 5679–5687.

Berenger, J. P. (1994), A perfectly matched layer for the absorption of electromagnetic waves, *J. Comput. Phys.*, *114*, 185–200.

Brocher, T. M. (2005), Empirical relations between elastic wavespeeds and density in the Earth's crust, *Bull. Seismol. Soc. Am.*, *95*(6), 2081–2092, doi:10.1785/0120050077.

Byerlee, J. (1978), Friction of rocks, *PAGEOPH*, *116*(4), 615–626, doi:10.1007/BF00876528.

Collino, R., and C. Tsogka (2001), Application of the PML absorbing layer model to the linear elastodynamic problem in anisotropic heterogeneous media, *Geophysics*, *66*, 294–307.

Das, S., and K. Aki (1977), A numerical study of two-dimensional spontaneous rupture propagation, *Geophys. J. Roy. Astron. Soc.*, *50*, 643–668.

Day, S. M. (1982), Three-dimensional simulation of spontaneous rupture: The effect of nonuniform prestress, *Bull. Seismol. Soc. Am.*, *72*, 1881–1902.

Day, S. M. (1998), Efficient simulation of constant Q using coarse-grained memory variables, *Bull. Seismol. Soc. Am.*, *88*, 1051–1062.

Day, S. M., L. A. Dalguer, N. Lapusta, and Y. Liu (2005), Comparison of finite difference and boundary integral solutions to three-dimensional spontaneous rupture, *J. Geophys. Res.*, *110*, B12307, doi:10.1029/2005JB003813.

Ding, Z., F. Romanelli, Y. T. Chen, and G. F. Panza (2004), Realistic modeling of seismic wave ground motion in Beijing City, *Pure Appl. Geophys.*, *161*(5–6), 1093–1106.

Di Toro, G., D. L. Goldsby, and T. E. Tullis (2004), Friction falls towards zero in quartz rock as slip velocity approaches seismic rates, *Nature*, *427*, 436–439, doi:10.1038/nature02249.

Duan, B. (2010), Role of initial stress rotations in rupture dynamics and ground motion: A case study with implications for the Wenchuan earthquake, *J. Geophys. Res.*, *115*, B05301, doi:10.1029/2009JB006750.

Duan, B. (2012), Dynamic rupture of the 2011 M_w 9.0 Tohoku-Oki earthquake: Roles of a possible subducting seamount, *J. Geophys. Res.*, *117*, B05311, doi:10.1029/2011JB009124.

Duan, B., and S. M. Day (2008), Inelastic strain distribution and seismic radiation from rupture of a fault kink, *J. Geophys. Res.*, *113*, B12311, doi:10.1029/2008JB005847.

Duan, B., and S. M. Day (2010), Sensitivity study of physical limits on ground motion at Yucca Mountain, *Bull. Seismol. Soc. Am.*, *100*(6), 2996–3019, doi:10.1785/0120090372.

Duan, B., and D. D. Oglesby (2006), Heterogeneous fault stresses from previous earthquakes and the effect on dynamics of parallel strike-slip faults, *J. Geophys. Res.*, *111*, B05309, doi:10.1029/2005JB004138.

Dunham, E. M., D. Belanger, L. Cong, and J. E. Kozdon (2011), Earthquake ruptures with strongly rate-weakening friction and off-fault plasticity, Part 2: Nonplanar faults, *Bull. Seismol. Soc. Am.*, *101*, 2308–2322, doi:10.1785/0120100076.

Harris, R. A., et al. (2009), The SCEC/USGS dynamic earthquake-rupture code verification exercise, *Seismol. Res. Lett.*, *80*(1), 119–126, doi:10.1785/gssrl.80.1.119.

Harris, R. A., et al. (2011), Verifying a computational method for predicting extreme ground motion, *Seismol. Res. Lett.*, *82*(5), 638–644, doi:10.1785/gssrl.85.5.638.

Ida, Y. (1972), Cohesive force across the top of a longitudinal shear crack and Griffith's specific surface energy, *J. Geophys. Res.*, *77*, 3796–3805.

Liu, C., B. Zhu, and Y. Shi (2016), Lithospheric rheology and Moho upheaval control the generation mechanism of the intraplate earthquakes in the North China Basin, *J. Asian Earth Sci.*, *121*, 153–164, doi:10.1016/j.jseaes.2016.03.008.

Liu, M., S. Stein, and H. Wang (2011), 2000 years of migrating earthquakes in North China: How earthquakes in midcontinents differ from those at plate boundaries, *Lithosphere*, *3*(2), 128, doi:10.1130/L129.1.

Liu, Q., and X. Li (2011), Broad-band strong motion simulation of the great Tangshan earthquake, *Earthq. Eng. Eng. Vib.*, *32*(5), 1–7.

Ma, S., and P. Liu (2006), Modeling of the perfectly matched layer absorbing boundaries and intrinsic attenuation in explicit finite-element methods, *Bull. Seismol. Soc. Am.*, *96*, 1779–1794.

Mai, P. M., and G. C. Beroza (2002), A spatial random field model to characterize complexity in earthquake slip, *J. Geophys. Res.*, *107*(B11), 2308, doi:10.1029/2001JB000588.

Olsen, K. B., S. M. Day, and C. R. Bradley (2003), Estimation of Q for long-period (>2 sec) waves in the Los Angeles Basin, *Bull. Seismol. Soc. Am.*, *93*(2), 627–638.

Olsen, K. B., S. M. Day, J. B. Minster, Y. Cui, A. Chourasia, D. Okaya, P. Maechling, and T. Jordan (2008), TeraShake2: Spontaneous rupture simulations of M_w 7.7 earthquakes on the southern San Andreas fault, *Bull. Seismol. Soc. Am.*, *98*(3), 1162–1185, doi:10.1785/0120070148.

Olsen, K. B., et al. (2009), Shakeout-D: Ground motion estimates using an ensemble of large earthquakes on the southern San Andreas fault with spontaneous rupture propagation, *Geophys. Res. Lett.*, *36*, L04303, doi:10.1029/2008GL036832.

Pan, B., J. Xu, S. Haruko, and H. He (2006), Simulation of the near-fault strong ground motion in Beijing region, *Seismol. Geol.*, *28*(4), 623–634.

Roten, D., K. B. Olsen, S. M. Day, Y. Cui, and D. Fah (2014), Expected seismic shaking in Los Angeles reduced by San Andreas fault zone plasticity, *Geophys. Res. Lett.*, *41*, 2769–2777, doi:10.1002/2014GL059411.

Scholz, C. H. (2002), *The Mechanics of Earthquakes and Faulting*, 2nd ed., pp. 17–21, Cambridge Univ. Press, Cambridge.

Shi, Z., and S. M. Day (2013), Rupture dynamics and ground motion from 3-D rough-fault simulations, *J. Geophys. Res. Solid Earth*, *118*, 1122–1141, doi:10.1002/jrgb.50094.

Wei, W., G.-F. Ye, S. Jin, M. Deng, and J. Jing (2007), Three dimensional *P*-wave velocity structure of the crust of North China, *Earth Sci. J. China Univ. Geosci.*, *32*(4), 441–452.

Yang, F., and J. L. Huang (2013), High precision 3D *P*-wave velocity model of the upper crust under the Chinese capital region based on oil seismic stack velocity and deep seismic sounding, *Chin. J. Geophys.*, *56*(5), 1487–1496, doi:10.6038/cjg20130507.

Ye, H., K. M. Shedlock, S. J. Hellinger, and J. G. Sclater (1985), The North China Basin: An example of a Cenozoic rifted intraplate basin, *Tectonics*, *4*(2), 153–169.

Yin, A., X. Yu, Z.-K. Shen, and J. Liu-Zeng (2014), A possible seismic gap and high earthquake hazard in the North China Basin, *Geology*, *43*(1), 19–22, doi:10.1130/G25986.1.

Zhou, H., and X. Chen (2008), Simulation of strong ground motion in Beijing city due to the Zhangbei earthquake, *Prog. Geophys.*, *23*(5), 1355–1366.